Highly selective and low-overpotential electrocatalytic CO_2 reduction to ethanol by Cu-single atoms decorated N-doped carbon dots

Rahul Purbia [a], Sung Yeol Choi [a], Chae Heon Woo [a], Jiho Jeon [a], Chulwan Lim [b], Dong Ki Lee [b,e], Jae Young Choi [a,b,c,*], Hyung-Suk Oh [b,c,**], Jeong Min Baik [a,c,d,*]

[a] School of Advanced Materials Science and Engineering, Sungkyunkwan University (SKKU), Suwon 16419, Republic of Korea
[b] Clean Energy Research Center, Korea Institute of Science and Technology, Hwarang-ro 14-gil 5, Seongbuk-gu, Seoul 02792, Republic of Korea
[c] KIST-SKKU Carbon-Neutral Research Center, Sungkyunkwan University (SKKU), Suwon 16419, Republic of Korea
[d] SKKU Institute of Energy Science and Technology (SIEST), Sungkyunkwan University, Suwon 16419, Republic of Korea
[e] Department of Chemical and Biochemical Engineering, Yonsei-KIST Convergence Research Institute, Yonsei University, Seoul 03722, Republic of Korea

ARTICLE INFO

ABSTRACT

Selective, low-overpotential and high Faradaic efficiency electroreduction of CO_2 to ethanol is in prominent global demand and lies in structuring, loading, and modulating the coordination states of Cu single atom catalysts (SACs) with support matrix. Here, the low-temperature (160 °C) synthesis of Cu–SACs–N-doped carbons dots (Cu–SACs–N–CQDs) is reported via Cu–dopamine complex process. The optimized Cu–SACs–N–CQDs electrocatalyst brings remarkably high Faraday efficiency (> 80%) and selectivity for ethanol with 50 h operation stability, which far exceeds previous results in terms of overpotential, stability, and Faraday efficiency. Surprisingly, the Faraday efficiency and selectivity of ethanol are highly sensitive to the coordination states of copper SACs with variation of Cu loadings. *Operando* X-ray absorption spectroscopy indicates in situ-generated neighboring metallic Cu–Cu atom coordination as real catalytic active sites from isolated single Cu atom during CO_2 reduction, which favors the ethanol selectivity.

1. Introduction

Carbon dioxide emissions have been nearly continuously increasing since the dawn of the industrial revolution. For CO_2 recycling, much attention has been paid to CO_2 electrochemical reduction to valuable chemicals as a promising prospect for solving issues related to the crisis of global warming and mandate for renewable energy.[1] Also, electrocatalytic CO_2 reduction reaction (CO_2 RR) offers the benefit of converting carbon dioxide to fuels at ambient temperature and pressure in the aqueous phase, compared to other conventional methods, like heterogeneous catalysis at elevated temperatures. It offers very attractive ways to address CO_2 emission in terms of selectivity, higher products, and renewable energy sources by facilitating the reduction of CO_2 molecules and electrochemical conversion to value-added chemicals (C_1–C_2).[2–4] Through CO_2 RR, CO_2 can be converted to C_1, C_2, or C_{2+} products via different proton- and electron-transfer steps and different CO_2 reduction pathways.[5–8] With the advantages of higher economic value and higher energy density, liquid-phase multi-carbon products (C_{2+} products, e.g., ethanol and acetate) are considered by the chemical industry to be more desirable products.[9–11] Among multi-carbon products, ethanol has prominent and wide global demand as a high-octane fuel and intermediate product in the various industries.

The consumption of ethanol has experienced significant growth in various industries over the last couple of decades, with applications ranging from industrial solvents, clean fuel and fuel additives to chemical feedstock, beverages, pharmaceuticals, and personal care products. Traditionally, ethanol has been primarily produced from corn, sugarcane, and grains. However, these conventional processes are associated with high energy requirements and CO_2 emissions. In response to the environmental challenges posed by traditional ethanol production methods, there has been increasing interest in the electrochemical conversion of CO_2 to ethanol. This approach aligns with the principles of a circular economy, aiming to close the carbon loop by transforming waste materials into valuable products. Electrochemical CO_2 conversion

to ethanol has the potential to contribute to the overall reduction of the carbon footprint associated with ethanol production. Given the large market size of ethanol, projected to reach approximately USD 162 billion by 2032 with an annual growth rate of 5.1%, the adoption of CO_2 electroreduction techniques for ethanol production becomes particularly valuable. This not only addresses the growing demand for ethanol but also promotes sustainability by mitigating energy-intensive processes and reducing CO_2 emissions [12–14].

Still, numerous electrocatalysts, such as metals, metal oxides, and carbon-based materials, have been designed for CO_2 RR. Among these numerous catalysts, copper (Cu) has the ability to generate multi-carbon products via oxygenating C−C coupling from CO_2 reduction. These multi-carbon products may be related to the optimal binding energy of CO intermediate on Cu, leading to the further reduction of CO intermediate, and achieving the C−C coupling. Typically, Cu-based electrocatalysts are composed of catalytically active sites, which mostly consist of bulk, nanomaterials, cluster, or single atom of metals supported by a conductive substrate. Although Cu-based catalysts can reduce CO_2 to C_2 (ethanol) products, the reduction still suffers from high barriers for CO_2 activation and C−C coupling, resulting in large overpotentials for C_2 product formation. In addition, ethanol and ethylene (C_2H_4) are the two mains competing C_2 products, because of their nearly theoretical overpotential and energy barrier [14–17].

To boost ethanol production, research interest has focused on Cu-based modifications, such as morphology, facet, vacancy steering, defects, dopant, and heterostructure engineering.[18–22] Owing to the maximum atomic utilization, controlled coordination environments, unique electronic properties, and low activation energy of metal catalytic active centers, Cu single-atom catalysts (Cu SACs) have demonstrated excellent selectivity in CO_2 RR reaction.[23–25] Though great progress has been achieved, previous Cu SACs studies are generally constrained to limited C−C coupling or selectivity over ethylene and high potential for ethanol production. However, higher negative potential could simultaneously overcome the high energy barrier of C−C coupling and enhance competitive hydrogen evolution. The promising key to boosting C−C coupling towards ethanol production at low overpotentials is to decrease the kinetic energy barrier of the C−C coupling process to construct the asymmetric interface sites of $Cu^{\delta+}$ and Cu^0 on the catalytic surface.[26–29] To solve this problem, researchers tried to immobilize Cu SACs on carbon supports to create heterogeneous catalytic surfaces.[12,22,30–32] In particular, N-doped carbon has proved to offer efficient N-anchoring sites for stabilizing metal atoms due to abundant N content and chemical stability, and therefore has been considered as an ideal support for single-atom catalysts. In general, there are two top-down and bottom-up strategies that have been widely used for synthesizing Cu SACs atoms on N-doped carbon supports. The top-down synthesis strategies include dispersion of Cu SACs atoms on the existing carbon supports (graphene or CNTs) or synthesized carbon. On the other hand, the bottom-up strategies include mixing of Cu metal and organic precursors, followed by a high-temperature carbonization process at (400−1000) °C to form the carbon matrix with Cu metal atoms embedded in carbon. Nevertheless, this strategy is limited to complex, high-cost, high-temperature, and low-yield synthesis SACs process methods with low selectivity, low efficiency, and low stability for ethanol production.[33] Therefore, developing single-atomic Cu catalysts with facile process and low-temperature with increased activity for ethanol selectivity is desirable.

In single-atomic catalysts synthesis, the metal anchored nitrogen-ligand plays crucial roles in tuning the electronic activity by modulating the coordination states of central metal atoms with carbon matrix, as the results affect the catalytic performance. Due to the complexity of the reaction and optimization, only a few studies have been reported in the field of metal anchoring ligand on carbon matrix. For example, metal precursor salt was combined with dicyandiamide[34] and organometallic amine complexes,[35] followed by annealing under inert atmosphere at (800−1000) °C temperatures on carbon support. Zhang et al.

reported a universal ligand-mediated method by complexing metal cations with 1,10–phenanthroline onto commercial carbon black, followed by at 600 °C temperature.[36] Similarly, graphene was stacked by Cu-incorporated aniline via π–π interactions by calcining at 400 °C.[37] Zhu et al. reported carbon-dots-based SAC via the calcination of copper disodium EDTA complex at 250 °C for 2 h.[23] However, it remains a grand challenge to stabilize metal anchored ligand in catalysts under a low-temperature and controlled coordinated environment.

Considering this, modulating the coordinated state of single-atom Cu–N moieties on carbon quantum dots (CQDs) can be a promising approach to develop a single-atom Cu isolated on N-doped carbons dots (N–CQDs) electrocatalyst. Herein, an isolated Cu single-atom on N-doped carbons dots (Cu–SACs–N–CQDs) electrocatalyst with unique Cu–N–C moieties by low-temperature hydrothermal methods has been successfully designed, where dopamine is used as an N- and Cu-anchoring source. The synthesis of N–CQDs supports of (2 −6) nm anchored with many isolated single-atoms Cu was confirmed by extended X-ray absorption fine structure (EXAFS), X-ray photoemission spectroscopy (XPS), and high-angle annular darkfield scanning transmission electron microscopy (HAADF−STEM). The Cu concentration is controlled by varying the metal–dopamine precursors to provide the spatial distribution of a single-atom catalyst. The Cu–SACs–N–CQDs catalyst exhibits a remarkable Faraday efficiency (> 70%), selectivity for boosted ethanol production, and decreased ethylene formation at low overpotential with stability over 50 h. In situ EXAFS during CO_2 reduction revealed that the single-atom Cu species provided catalytic active sites for CO_2 electroreduction to ethanol. Additionally, using *operando* XAFS, a positive correlation between the isolated Cu atoms with anchoring agent and the selectivity of C_{2+} products was demonstrated, where an isolated Cu is rapidly reduced to metallic Cu under CO_2 RR to favor remarkable electrocatalytic C_{2+} products formation at low overpotential. Thus, these electrocatalysts are demonstrated as being highly efficient and highly selective towards the formation of ethanol during electrocatalytic CO_2 reduction.

2. Experimental section

2.1. Materials

Dopamine hydrochloride, citric acid, copper acetate, copper (II) chloride, KOH and $KHCO_3$ were obtained from Sigma–Aldrich. All these chemicals were of reagent grade and were used without further purification.

2.2. Preparation of Cu-SACs-N-CQDs

The synthetic strategy of Cu-SACs-N-CQDs is described in Fig. 1. Firstly, dopamine hydrochloride (0.125 g) and certain amount of $CuCl_2$ were dissolved in 80 mL of ethanol and water mixture (1:1). The suspension could disperse uniformly under vigorous stirring to ensure a strong interaction between dopamine and Cu^{2+}. Then, citric acid (0.5 g) was added to above suspension. Next, the dispersion was transferred into a 100 mL Teflon-lined stainless-steel autoclave and heated at 160 °C for 6 h. After reaction, the autoclave was allowed to cool to room temperature naturally. Next, the dispersion was filtered using a dialysis membrane of 10k molecular weight cut-off (MWCO) to remove the unanchored Cu^{2+} ions and unreacted dopamine. The above solutions were again filtered by a syringe filtration membrane filter (0.22 μm) and freeze dried to get powder after dialysis membrane. The synthesized Cu-SACs-N-CQDs catalyst was denoted as per its dopamine contents during synthesis reaction. The catalyst was denoted as Cu-SACs-1 N-CQDs (0.125 g dopamine), Cu-SACs-2 N-CQDs (0.500 g dopamine) and Cu-SACs-3 N-CQDs (1.00 g dopamine).
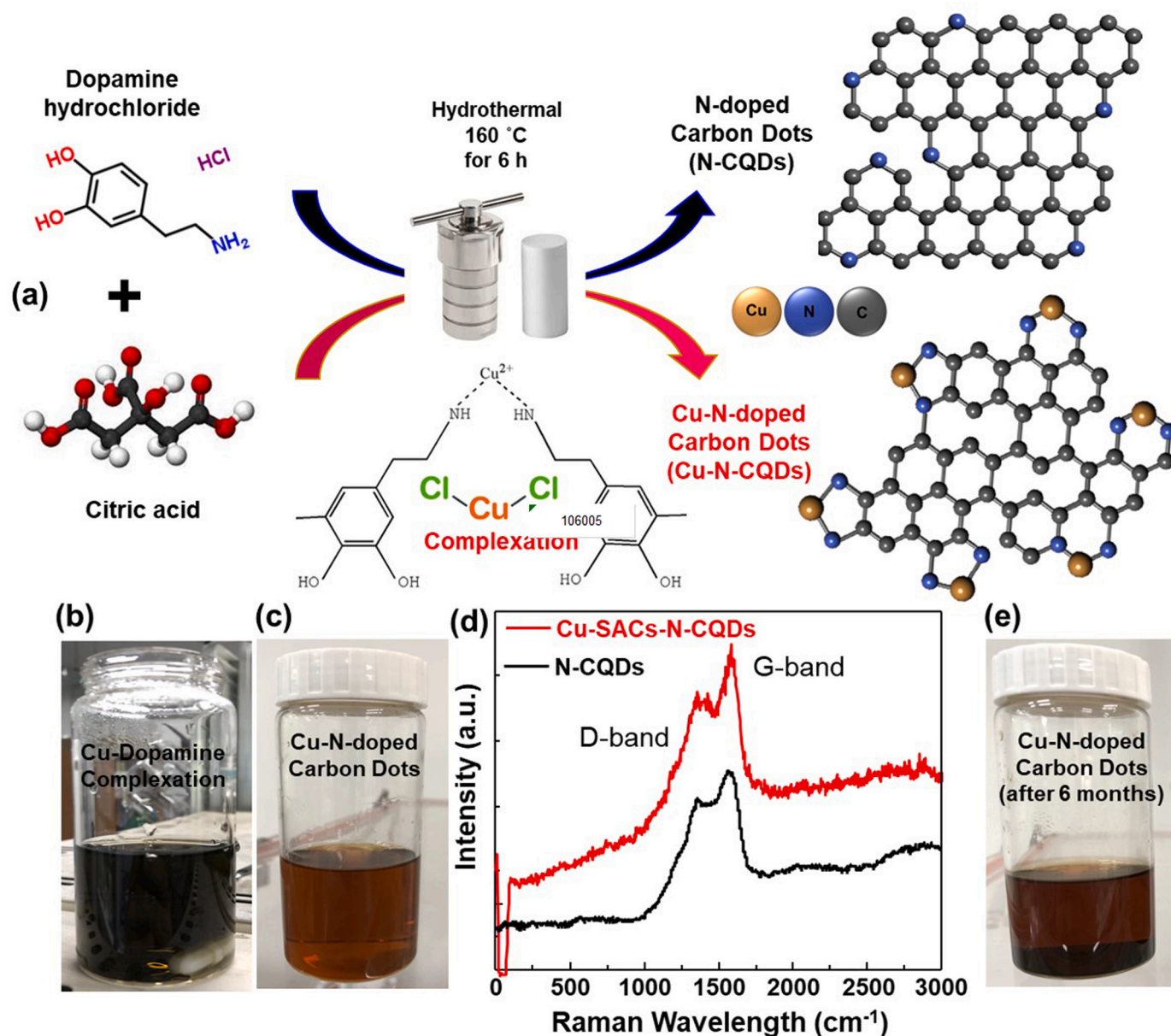
Fig. 1. Overall synthesis process for the Cu–SACs–N–CQDs electrocatalyst (a) synthesis process, (b) Cu-dopamine complexation physical appearance, (c) synthesized Cu–SACs–N–CQDs solution physical appearance, (d) Raman spectra of N–CQDs and Cu–SACs–N–CQDs, (e) physical appearance and stability of Cu–SACs–N–CQDs after 6 months.

2.3. Instrumentation

The structural morphologies of the catalyst materials were investigated using scanning electron microscopy (SEM, Jeol JSM-6700 F) and transmission electron microscopy equipped with energy-dispersive X-ray spectroscopy (TEM, JEOL JEM-2100 F). X-ray photoelectron spectroscopy (XPS, Thermo Fisher K-alpha) was conducted to obtain surface information and the bonding states of the elements. Binding energies of all XPS spectra were calibrated by the C 1 s binding energy of adventitious carbon contamination which was taken to be 284.8 eV. Raman spectra were performed by Rennishaw InVia spectrometry (INVIA RE-FLEX) with 514.5 nm laser excitation.

2.4. Electrochemical measurements

All electrochemical measurements were conducted on an Ivium nStat electrochemical workstation in a standard three-electrode system with an H-cell configuration. The as-prepared electrode served as the working electrode, Ag/AgCl electrode with saturated KCl solution served as the reference electrode, and the Pt mesh served as the counter electrode. A 50 mL 0.1 M KHCO$_3$ solution was used in both cathode and anode compartments as electrolyte, which was bubbled with CO$_2$ gas (1.0 atm, 99.95%) through the mass-flow controller. The anode and cathode compartments were separated by a Nafion–117 proton exchange membrane. Linear sweep voltammograms (LSVs) were recorded by electrochemical workstation. All potentials in this work were converted to reversible hydrogen electrode (RHE) by the following Nernst equation:

$$E(RHE) = E(Ag/AgCl) + 0.199 + 0.059 \times pH$$

The practical availability of the Cu-SACs-N-CQDs catalyst towards a large-scale CO$_2$ electrolysis was evaluated with a flow cell membrane electrode assembly (MEA)-based electrolyzer. For MEA cell measurements, a GDE loading with Cu-SACs-1 N-CQDs catalyst, and a Ni mesh were applied as the cathode and anode, respectively, where an anion

exchange membrane (AEM) was sandwiched between the two electrodes. Such a compact sandwich structure makes the electrodes achieve "zero-gap", lowering the ohmic losses to the greatest extent. The humidified CO_2 (500 sccm) flowed to the cathode compartment by a flow controller and 1 M KOH was recirculated through the anode compartment at a flow rate of 20 mL/min using a peristaltic pump.

2.5. Product analysis and Faraday efficiency calculation

Liquid reduction products were detected via ^1H NMR spectra using a Unity Inova spectrometer of Varian Technology (500 MHz). The catholyte solution (500 μL) containing the liquid product was mixed with the D_2O solution (100 μL) of contains 0.05 wt% 3-(trimethylsilyl)propionic-2,2,3,3-d$_4$ acid sodium salt (TMS) as internal reference standards. The relative area of ^1H NMR peaks for liquid products was used to quantify the concentration of the liquid products by using the standard calibration curve of pure products. Gas-phase reduction products were detected by gas chromatography (Shimadzu GC-2010 Pro). The Faraday efficiency of ethanol (C_2H_5OH) was calculated from the total amount of charge (Q/C) passed through the sample and the total amount of C_2H_5OH (nC_2H_5OH/mol). Q=I×t, where I is the current at specific applied potentials, and t is the time for constant reduction currents. As 12 electrons are needed to generate one C_2H_5OH molecule, the Faraday efficiency can be calculated by the following equation:

Faraday efficiency = 12 F × n C_2H_5OH / (I×t),

where, F is the Faraday constant (96,485 C/mol).

2.6. Operando studies

The in situ/Operando XAFS measurements of Cu–K-edges were conducted in fluorescence mode at the 1D beamline of the Pohang Accelerator Laboratory (PAL), Pohang, South Korea. A custom-made CO_2 H-cell with a small hole was used for this purpose. At each current density, the device was stabilized for 10 min before the XAFS measurements. All recorded raw data were processed using the Athena and Artemis software version 0.9.26, including the Demeter package.

3. Results and discussion

3.1. Synthesis and characterization of the Cu–SACs–N–CQDs catalyst

Fig. 1 and S1 of the Supporting Information (SI), depict the synthetic strategy of the Cu–SACs–N–CQDs. To experimentally construct the Cu–SACs–N–CQDs, we developed a Cu metal–dopamine complex method, where Cu sources could be incorporated by dopamine molecules, which also provide nitrogen anchoring sources to make the high-density N-anchored Cu–SACs. The Cu–SACs–N–CQDs were synthesized by complexing dopamine and Cu precursors ($CuCl_2$ and $Cu(Ac)_2$) with citric acid, followed by hydrothermal reaction at 160 °C for 6 h (Fig. 1a). In the hydrothermal process, Cu^{2+} ions were initially coordinated with dopamine to form a Cu-dopamine complex (Fig. 1b), with Cu atoms being isolated within metal-ligand (amine) assemblies. Subsequently, via thermal polymerization and carbonization reactions, Cu species underwent atomic dispersion, coordinating with nitrogen (N) atoms of carbon dots. This led to the in-situ formation of Cu-N-C sites in the solution (Fig. 1c). The resulting catalyst structure is depicted in Fig. 1a. The atomic coordination number can be adjusted by varying the concentration of dopamine during the synthesis of the Cu-SACs-N-CQDs catalyst. The Cu–SACs–N–CQDs solution showed excellent stability over six months without agglomeration, as shown in Fig. 1e and Fig. S2 of the SI.

To describe the structure of Cu–SACs–N–CQDs catalyst, the X-ray diffraction (XRD) and Fourier-transform infrared spectroscopy (FT-IR) spectra are employed to determine the structure and functional groups

of the Cu-SACs-N-CQDs catalysts, as shown in Figs. S3a and S3b of the SI, respectively. The XRD spectra of Cu-SACs-1 N-CQDs showed too broad peaks for N-CQDs due to small nanocrystals or quantum size particles with a size below 5 nm. Also, No Cu peaks appeared in the XRD patterns corroborated the successful synthesis of the Cu-SACs-1 N-CQDs. The FTIR of Cu-SACs-1 N-CQDs showed that the -OH stretching (≈ 3490 cm^{-1}), C-H stretching (≈ 2970 cm^{-1}), C=O/C=N (≈ 1597 cm^{-1}), C-O-C (≈ 1140 cm^{-1}) stretching are present. The C=N (≈ 1600 cm^{-1}), and C-N (≈ 1390 cm^{-1}) stretching emerge in Cu-SACs-N-CQDs, which confirms the presence of N in quantum dots. FTIR results revealed the presence of nitrogen-containing molecules groups in Cu-SACs-N-CQDs. Fig. 1d also presents the Raman spectrum of the Cu–SACs–N–CQDs, which shows two distinct peaks at (1390 and 1622) cm^{-1} (D-band and G-band), respectively. The G-band (sp^2 hybridization) represents the amount of graphitization associated with the N–CQDs, while the D-band (sp^3 hybridization) represents the amount of defect and degree of functionalization.

The molecule of dopamine contains one amino and two phenolate (hydroxyl) sites as basic centers. The Cu(II) chelates with dopamine and coordinated in a tridentate manner with O-N-O donor sites of the phenolic–OH, and –NH. In acidic or neutral conditions, the nitrogen atom is protonated forming a pyridinium ion with a positive charge on nitrogen. [38,39] The positively charged nitrogen attracts electrons to a greater extent and results in greater chance for metal chelation complex. [40–44] However, the surface hydroxyl (–OH) groups of dopamine preferentially undergo polymerization with surface hydroxyl (–OH) groups of citric acid followed by carbonization to form Carbon dots under hydrothermal reaction. Thus, the interaction between Cu and N atoms is deeply analyzed in Cu-SACs-1 N-CQDs coordination.

To understand the electronic structure of the synthesized catalyst with Cu precursors ($CuCl_2$ and $Cu(Ac)_2$), X-ray photoelectron spectroscopy (XPS) and scanning electron microscopy (SEM) equipped with energy dispersive spectrometry (EDS) measurement were performed with different Cu precursors ($CuCl_2$ and $Cu(Ac)_2$), as shown in Fig. 2, and Fig. S4 of the SI, respectively. Binding energies of all XPS spectra were calibrated by the C 1 s binding energy of adventitious carbon contamination which was taken to be 284.8 eV. As expected, the XPS spectra of the pure N–CQDs without a Cu source revealed the presence of C and N elements. From the C 1 s spectra (Fig. 2a), the deconvoluted C 1 s peak reveals the major content of C=C sp^2 (283.7), C–C sp^3 (284.7), N–C=N species (286.7 eV), C–O or C=O (289.7 eV), and π–π * shake-up satellite peak of sp^2 carbon (289.7 eV). The pure N–CQDs also exhibit single nitrogen-containing functional groups peaks related to graphitic N (400.5 eV), as shown in Fig. 2b. As the Cu was introduced, the XPS spectrum validated the presence of C, N, and Cu elements on the Cu–SACs–N–CQDs with different Cu precursors. With $CuCl_2$ as a Cu precursor, the N 1 s in Cu–SACs–N–CQDs was shifted toward lower binding energy and showed different deconvoluted peaks, suggesting that the coordination environment of N–CQDs was changed. Three components of Cu–N species (398.6 eV), graphitic N bond (399.7 eV), and oxidized N species (401.1 eV) can be deconvoluted from the N 1 s spectra. In the Cu 2p spectra (Fig. 2c), the Cu 2p$_{3/2}$ and Cu 2p$_{1/2}$ peaks are deconvoluted into two separate peaks with binding energies of (932.7/934.3 and 952.5/954.1) eV, respectively, which can be assigned to Cu^0 or Cu$^+$, and Cu^{2+} state, respectively. With the absence of satellite peaks, the Cu 2p$_{3/2}$ peak was made up of two peaks of Cu^0 or Cu$^+$ (932.7 eV) and Cu^{2+} (934.3 eV), suggesting a special valence state (Cu$^{\delta+}$) due to the coordination environment of Cu–N. The combined Cu 2p spectra with spectrum exhibited that the Cu atoms were positive-charged on the Cu–N–C surface, indicating the typical state of single-site Cu structure. The existence of positive-charged Cu species could be attributed to the strong interaction from the surface Cu–N structures. The binding-energy shifts as per the Cu precursors of Cu 2p and N 1 s indicated that the electronic state of Cu and N atoms changed because of the coordination of N-doped carbon dots and the Cu–SACs.

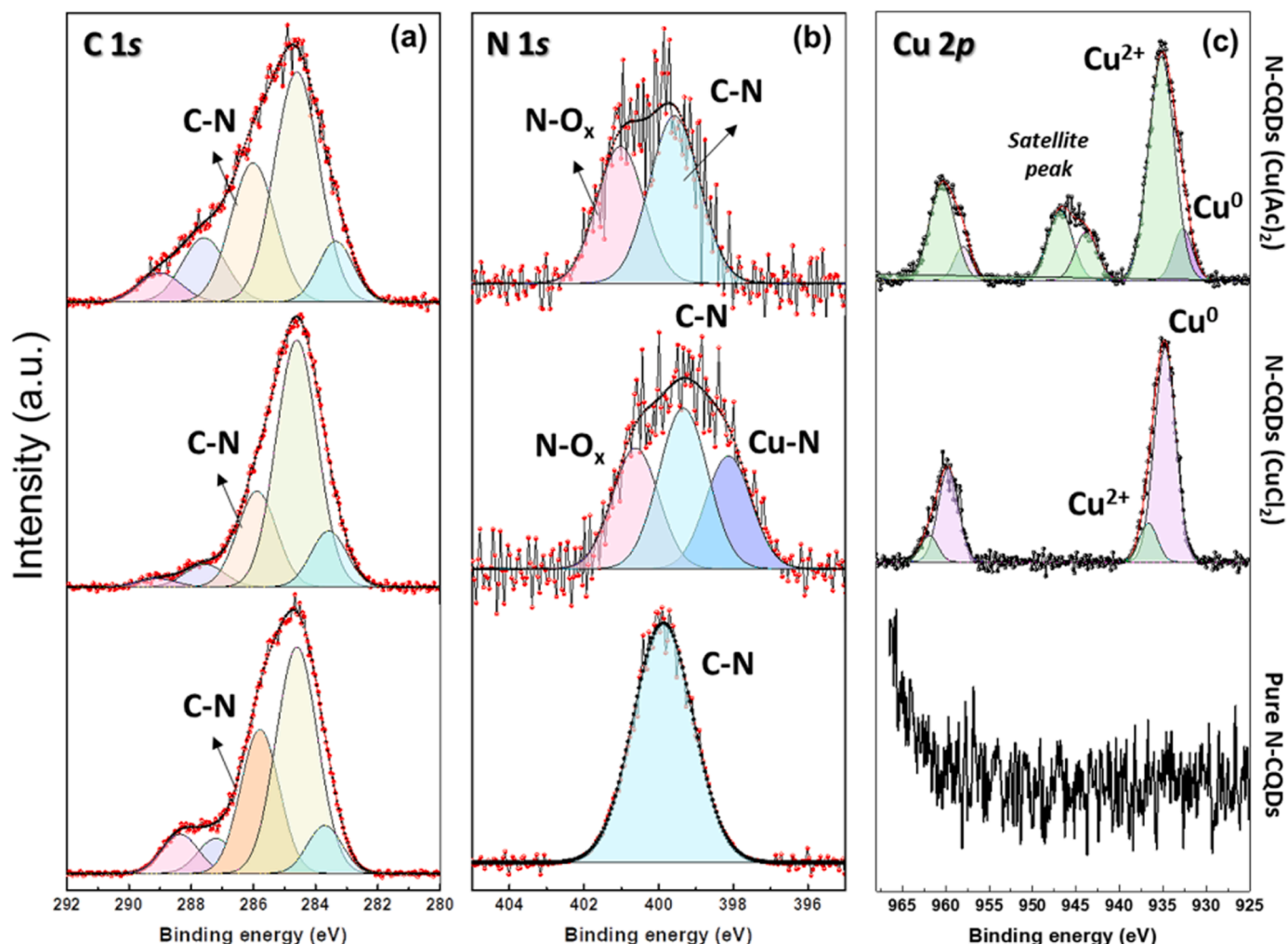However, with $Cu(Ac)_2$ precursor, the deconvoluted N 1 s spectrum

Fig. 2. (a)–(c) XPS spectra characterization of the N − CD, Cu–SACs–N–CQDs (CuCl$_2$), and Cu–SACs–N–CQDs (Cu acetate).

only showed the major species of graphitic N bond (399.7 eV) and oxidized N species (401.1 eV). Similarly, the Cu 2p$_{3/2}$ and Cu 2p$_{1/2}$ peaks are deconvoluted into two separate peaks with binding energies of (931.2/932.9 and 951.1/952.9) eV, which are assigned to the Cu$^+$ and Cu^{2+} states, respectively. Also, the two additional peaks around (943 − 946) eV in the Cu 2p$_{3/2}$ peak region result from a shake-up peak due the existence of a Cu^{2+} state, indicating the formation of CuO clusters in the Cu–SACs–N–CQDs. Overall, the Cu–SACs–N–CQDs prepared using CuCl$_2$ precursor contained Cu–N moieties and oxidized Cu state, while the Cu–SACs–N–CQDs prepared using Cu(Ac)$_2$ revealed the highest concentration of CuO and the absence of Cu–N moieties. This difference in precursors composition resulted in the different coordination environment of Cu–N. Based on the XPS results, CuCl$_2$ precursors were used to prepare Cu–SACs–N–CQDs catalyst due to Cu–N moieties and the better coordination environment of Cu–N–C.

To further investigate the electronic properties, optimization parameters, and coordination environment of the Cu–SACs–N–CQDs, XPS measurement was performed with different dopamine concentration (Fig. S5 of the SI). To avoid the interference of metal loading on activity, the feeding of inorganic copper (CuCl$_2$) and citric acid sources was kept the same, while the dopamine concentration was changed, and analyzed by XPS (Fig. S5 of the SI). With increase in dopamine concentration from (0.125 to 0.500) g, the corresponding Cu^0 or Cu^{2+} state, and Cu–N moieties peak content increases without satellite peaks, suggesting the SACs-like coordination environment of Cu–N. While with 1.0 g dopamine concentration, the satellite peaks appeared with Cu^0 or Cu^{2+} state,

and Cu–N moieties, indicating the formation of CuO atomic clusters in the Cu–SACs–N–CQDs. Thus, higher dopamine concentration tends toward the formation of Cu atomic cluster, while low dopamine concentration provides a SACs-like coordination environment. Fig. 3 shows a representative EDS analysis of different dopamine contents. It is shown that with increase in dopamine contents, the Cu loading was increased first and then decreased, in agreement with the XPS analysis (Fig. S5 of the SI). A representative HAADF−STEM image (Fig. S6 of the SI) shows all the Cu species existing exclusively as isolated single atom with 0.125 g dopamine contents (Cu–SACs–1 N–CQDs). With increasing dopamine contents to 0.500 g, some larger Cu atomic clusters with isolated single atom were detected at Cu–SACs–2 N–CQDs (0.500 g dopamine). However, the Cu–SACs–3 N–CQDs (1.00 g dopamine) showed mostly larger Cu atomic clusters (Fig. S6 of the SI), supporting the XPS analysis. Based on the XPS, TEM, and EDS analyses, we found the 0.125 dopamine synthesized Cu–SACs–N–CQDs (Cu–SACs–1 N–CQDs) as providing the optimum concentration to obtain the isolated Cu single atom, and further used it for detailed analysis.

Low-magnification transmission electron microscopy (TEM) images (Fig. 4a-b) show that the Cu–SACs–1 N–CQDs had an average diameter of (2 −6) nm, quite similar in size to the pristine N–CQDs of Fig. S1b of the SI. The narrow distribution of the diameter suggests that the Cu–SACs–N–CQDs have a relatively uniform size distribution within that range. The Cu–SACs–1 N–CQDs were also well-dispersed. High-resolution TEM (HR−TEM) imagery of the Cu–SACs–1 N–CQDs measures the lattice fringe to be ~0.21 nm from the N–CQDs (Fig. 4c), which is in
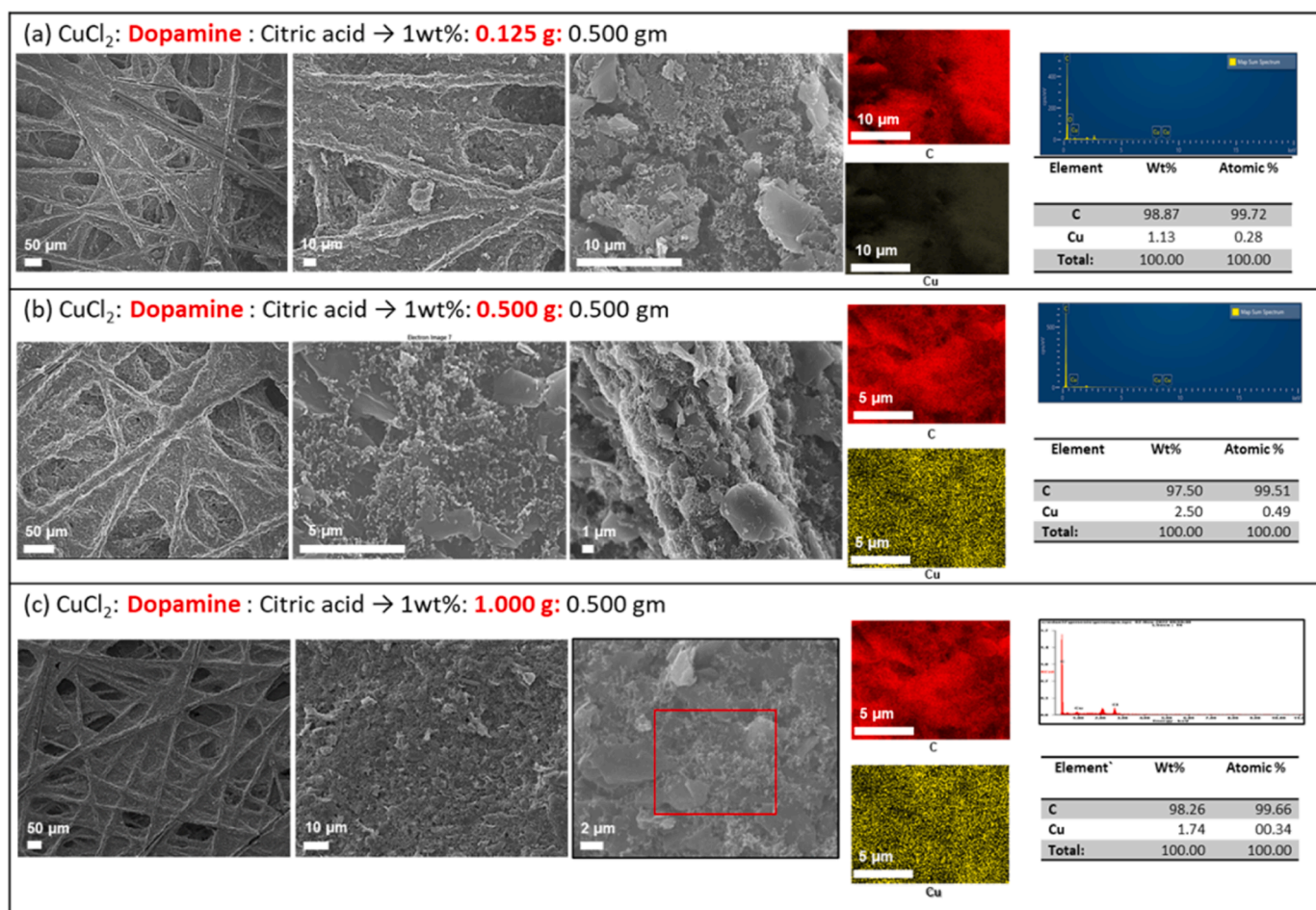
Fig. 3. SEM and EDS analysis of the deposited catalyst on Carbon paper with different dopamine (Cu–SACs–N–CQDs) contents (scale bar left to right (a) 50 μm, 10 μm, 10 μm, 10 μm (C), 10 μm (Cu), (b) 50 μm, 5 μm, 1 μm. 5 μm (C), 5 μm (Cu), (c) 50 μm, 10 μm, 2 μm, 5 μm (C), 5 μm (Cu).

good agreement with the (100) interplanar spacing of the pristine N–CQDs. The fast Fourier transform (FFT) pattern, as shown in Fig. 4d, reveals two concentric rings with diffraction radii of ~ (0.21 and 0.17) nm, corresponding to the (100) and (002) planes of graphite-like carbon, respectively. Thus, the atomic imagery could not find the presence of the Cu elements, or any aggregates related to the Cu elements in the product.

For further investigation of the Cu elements in the Cu–SACs–N–CQDs, aberration-corrected high-angle annular dark-field scanning TEM (HAADF−STEM) with a contrast proportional to the square of the atomic number (Z^2) was employed. As shown in Fig. 4e–g, discrete bright dots (yellow circles) could be observed in the whole image, indicating that Cu atoms are atomically anchored into the N-doped carbon dots. The particle size of Cu atoms was assumed to be about sub-angstrom range, revealing that Cu on N–CQDs was present at the atomic dimension. Actually, it is extremely difficult to capture HAADF−STEM images of the Cu–SACs–N–CQDs, due to their intrinsic fragile nature and carbon contamination under the convergent electron beam. However, EDS mapping analysis in STEM images of the Cu–SACs–1 N–CQDs (Fig. S7 of the SI) suggests that the Cu was detected, and uniformly dispersed on N–CQDs, verifying that N-doped carbons dots were formed during hydrothermal reaction, and served as a carrier for the Cu–N species. The result of discrete bright dots, high contrast of isolated Cu atoms, and STEM−EDS mapping were in good agreement with the HRTEM analysis.

At low dopamine concentrations, nitrogen atoms from the carbon source (dopamine) play a crucial role in stabilizing single Cu atoms through the formation of the Cu-N coordination configuration, particularly chelating in acidic or neutral conditions. Due to the anchoring effect at low dopamine levels, the incorporated nitrogen sites demonstrate a substantial ability to coordinate with metal ions. Under hydrothermal conditions, the complex undergoes polymerization and carbonization reactions, ultimately yielding the Cu-SACs-N-CQDs catalyst. However, an increase in dopamine concentration significantly accelerates the oxidative polymerization of dopamine in the hydrothermal environment. This acceleration initiates with the transformation of dopamine (catechol moieties) into the corresponding dopamine-o-quinone moieties via an oxidation reaction.[45–50].

To further investigate the electronic properties and coordination environment of the Cu–SACs–N–CQDs, X-ray absorption near-edge spectroscopy (XANES) and X-ray absorption fine structure (XAFS) measurements were performed to gain insight into the interface structure of the Cu–SACs–N–CQDs at atomic scale. The average oxidation state of Cu species can be described through the adsorption threshold of the Cu–K-edge. Fig. 5a shows the Cu–K-edge XANES profiles for the measured Cu–SACs–N–CQDs sample and the related references (pure Cu, Cu(II) phthalocyanine (CuPc), and Na2[Cu(EDTA)]). The Cu–SACs–1 N–CQDs exhibit an energy absorption edge between Cu^{2+} (CuPc) and Cu^{2+} (Cu(EDTA)) standards in the range of E_0 (around 8978 eV) as shown in Fig. S9 of the SI, further verifying that the oxidation state of Cu between the two reference structures and the Cu ion is coordinated with N–ligation. This signal was thought to be derived from the Cu–SACs–1 N–CQDs, providing accurate evidence for the formation of Cu–N bonding in the form of isolated Cu single atoms in the Cu–N–C–QDs. However, the Cu–SACs–3 N–CQDs catalyst shows a similar Cu–K-edge XANES spectrum to compound pure Cu and CuPc,
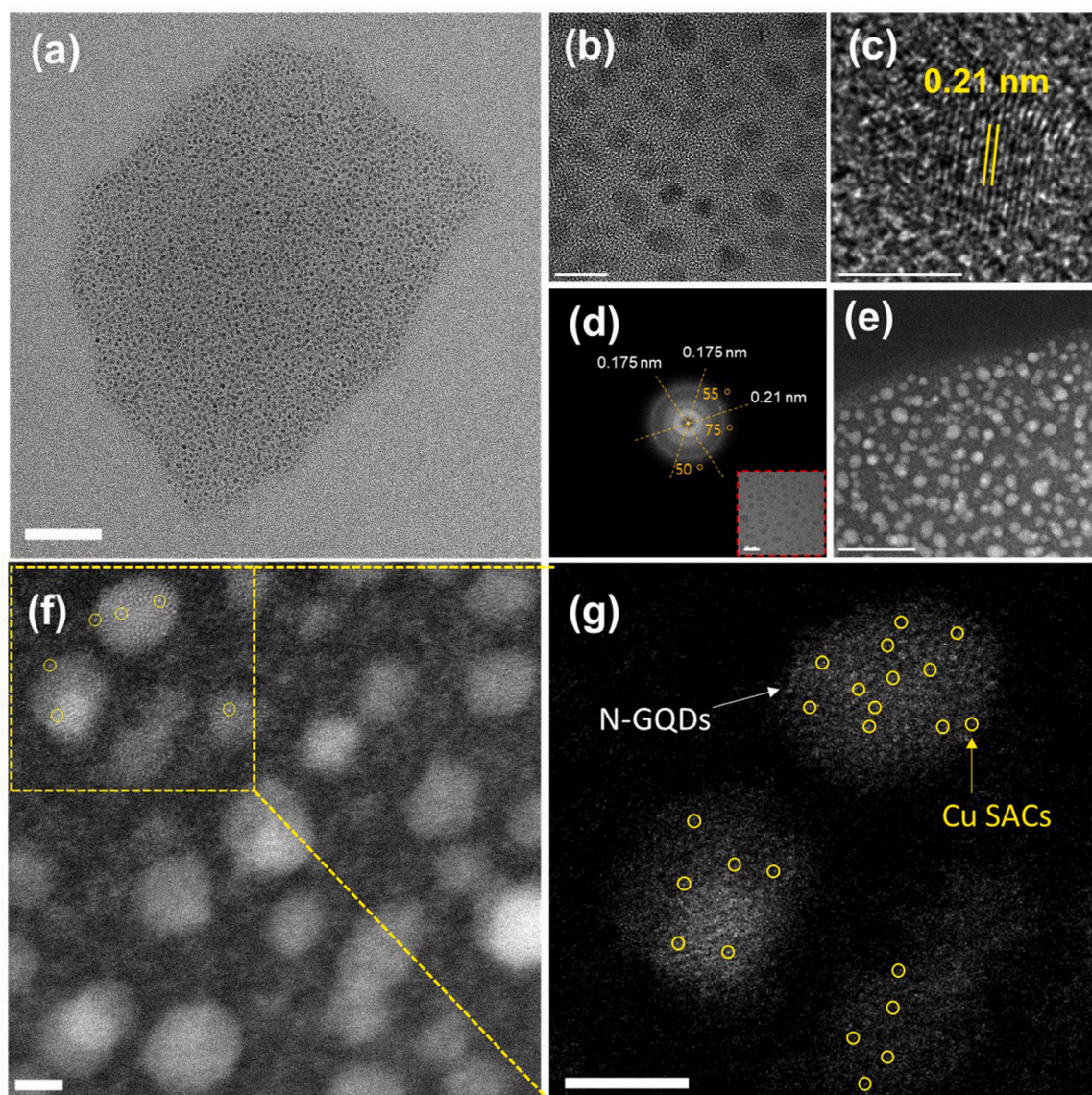
Fig. 4. (a)–(c) HRTEM image, (d) FFT pattern of inset HR−TEM image, (e)–(g) HAADF−STEM image of all the Cu species on the carbon-dots Cu–N–CQDs (scale bar: (a, g) 50 nm, (b) 10 nm, (c) 2 nm, (d, e) 20 nm, (f, g) 2 nm).

verifying metallic Cu cluster or oxidized CuOx clusters with higher dopamine contents.

Further, the coordinative geometry of the Cu–SACs–N–CQDs was analyzed by Fourier transform extended X-ray absorption fine structure (FT−EXAFS), as shown in Fig. 5**b**. In agreement with the XANES data analysis, the shape of the post-edge in the Cu–SACs–N–CQDs is vastly different from that of the pure Cu, Cu(II) phthalocyanine (CuPc), and Na_2[Cu(EDTA)]), indicating the disparate coordinative structure of the Cu–SACs–N–CQDs, as depicted in the extended X-ray absorption fine structure (EXAFS) in Fig. 5**b**. The EXAFS spectra (Fig. 5**b**) for the Cu–SACs–1 N–CQDs display a prominent peak at approximately (1.5 − 1.9) A° corresponding to Cu–N structural motifs, and no significant contribution for metallic Cu or oxidized CuOx clusters at longer distances above 2.1 A° is observed, revealing the atomic dispersion of isolated Cu atoms throughout the 1 N–CQDs matrix. Meanwhile, the Cu–SACs–3 N–CQDs EXAFS spectra display a prominent peak at approximately 1.5 A°, and two significant contributions for metallic Cu or oxidized CuOx clusters at longer distances above 2.1 A° are observed, revealing the atomic dispersion of isolated Cu atoms with Cu atomic clusters throughout the N–CQDs matrix. Finally, the near-edge of the

Cu–SACs–1 N–CQDs and Cu–SACs–3 N–CQDs (Fig. 5**b**) features obviously different shapes, implying the possible difference in coordination environment of single-atom Cu moieties with different dopamine concentration during reaction. This provides solid evidence that N atoms anchor Cu on the carbon dots to form single atomic sites with 0.125 g dopamine contents, which was earlier validated by the XPS and TEM results.

3.2. Catalytic evaluation

The CO_2RR performances of the Cu–SACs–N–CQDs catalysts were evaluated by linear sweep voltammetry (LSV), cyclic voltammetry, and chronoamperometry in a standard three-electrode system with an H-cell configuration and 0.1 M $KHCO_3$ electrolyte solution (Fig. 6). Before electrochemical study, the Cu–SACs–N–CQDs were deposited on the carbon paper, as seen in Fig. 6**a–c**. Then, the potential-dependent selectivity for CO_2RR products of the Cu SACs–1 N–CQDs catalysts was analyzed in the range of different Cu wt% loading (Fig. 6**d**). Compared with the carbon paper, as 1 wt% Cu was loaded, the current density was significantly increased, however, further increase in the Cu
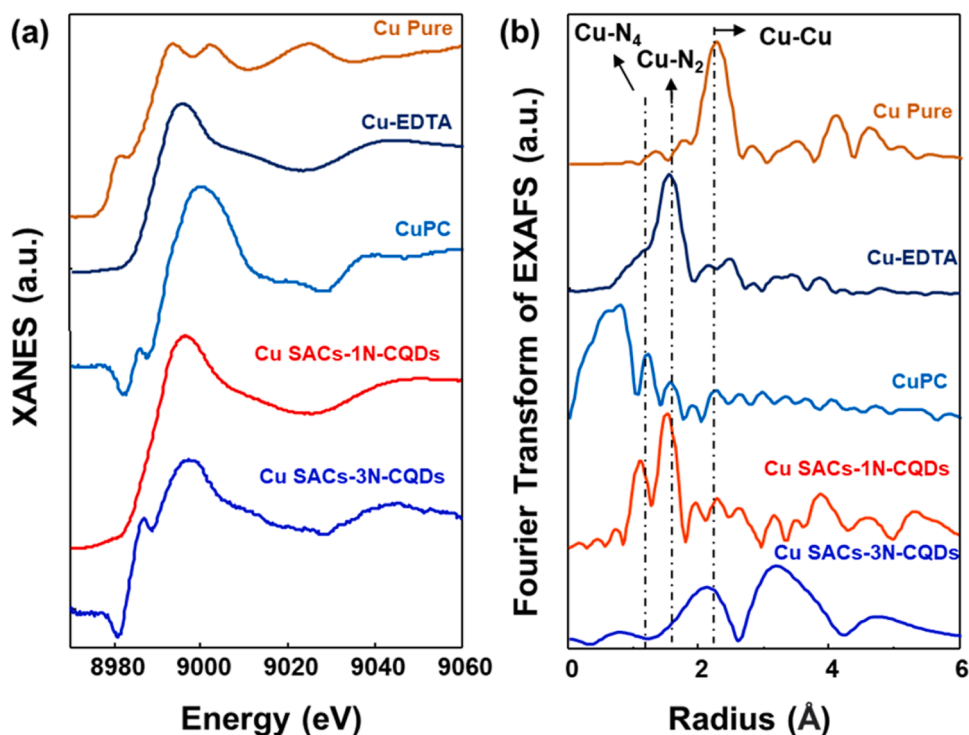
Fig. 5. XANES spectra characterization. (a) The XANES spectra at the Cu–K edge, and (b) Fourier transform of the experimental EXAFS spectra.

content up to 10 wt% decreased the current density. Similarly, with a fixed Cu content of 1 wt%, the potential-dependent selectivity for CO_2RR products of the Cu-SACs-N-CQDs catalysts was analyzed in the range of different dopamine wt% loading on Cu-SACs-N-CQDs catalysts (Fig. 6e). The largest current density was observed in Cu-SACs-2 N-CQDs (0.500 g dopamine) loading on N-CQDs catalysts compared to Cu-SACs-1 N-CQDs (0.125 g dopamine) and Cu-SACs-3 N-CQDs (1.0 g dopamine).

Fig. 6f shows the FEs and CO_2 RR product distributions as the function of applied potentials from (−0.2 to −0.6 V (RHE)) based on the nuclear magnetic resonance (NMR) spectra and gas chromatography (GC) analysis. As shown in Fig. 4f, and Fig. S10-S11 of the SI, the products mainly contain H_2, C_2H_4 in the gaseous phase, and ethanol in the liquid phase, respectively. The Cu–SACs–1 N–CQDs catalyst exhibits excellent selectivity toward C_{2+} products at low overpotentials and achieves a maximum $FE_{ethanol}$ of 70% with a total current density of 1.0 mA m^{-2} at − 0.2 V (RHE). No appreciable decays of current density, nor structural changes (Fig. 6i) after a 50 h continuous test at − 0.2 to − 0.3 V are observed, indicating the excellent stability and potential for practical application of the Cu–SACs–1 N–CQDs catalyst. Also, the liquid collected of Cu–SACs–1 N–CQDs catalyst at different time-intervals during continuous test with (5, 18, 30 and 50) h reaction time exhibits NMR-based $FE_{ethanol}$ of (70%, 74%, 80% and 75%), respectively (Fig. 6i). The SEM and TEM analysis of the catalysts after long-term stability during 50 h showed that the morphology remained intact without any visible aggregates and good dispersion with proper Cu elements contents, as shown in Fig. S12. Table S1 of the SI compares the applied potential and $FE_{ethanol}$ between this work and other previously reported Cu-based catalysts with ethanol and suggests that the construction of the Cu–SACs–1 N–CQDs interface sites with the asymmetric electronic structure center provides an efficient strategy to develop ethanol selective electrocatalysts at low overpotential. The Cu-SACs-1 N-CQDs catalyst was also evaluated with a MEA-based electrolyzer for a large-scale CO_2 electrolysis. The CO_2 reduction performance and stability of the MEA cell equipped with Cu-SACs-1 N-CQDs catalyst is shown in Fig. S13. The linear sweep voltammetry curves for optimized

Cu-SACs-1 N-CQDs electrode showed that the current density for CO_2 reduction of Cu-SACs-1 N-CQDs were significantly increased to 30 mA·cm^{-2}, directly evidencing that flow cell configuration modification boosted activity for CO_2 reduction. During chronopotentiometry at constant − 0.2 V (vs. RHE), the liquid products were collected and analyzed through NMR and found similar FE values (69%) of ethanol products on the Cu-SACs-1 N-CQDs catalyst like H-cell with better current density.

3.3. In situ operando XAFS during the CO_2 reduction reaction

To further monitor the local Cu atoms coordination environment, operando X-ray absorption spectroscopy (XAS) of Cu-SACs-1 N-CQDs (0.125 g dopamine) and Cu-SACs-3 N-CQDs (1.0 g dopamine) were carried out under real electrochemical CO_2RR conditions, as shown in Fig. 7 and Fig. S14 of SI. Unless specifically noted, all applied voltages in this work are referred to as the reversible hydrogen electrode (RHE). In the XANES spectra (Fig. S14 of SI), the Cu K-edge adsorption position of Cu-SACs-N-CQDs were lower shifted from ~8985 eV to ~8981 eV with applied negative potentials, indicative of a change of the Cu local oxidation state to reduced Cu species. Consistently, Fourier transformed (FT) Cu K-edge EXAFS spectra (Fig. 7a-b) measured under operating conditions also demonstrated the rapid reduction of Cu-N to metallic Cu−Cu atom coordination with applied negative potential. With the applied potential moving more negatively, it can be seen that the Cu−N coordination number decreases with decreased corresponding Cu−N peaks (1.5−1.9 Å) intensity while neighboring Cu−Cu atom coordination took place as corresponding metallic Cu (2.1−2.2 Å) peaks significantly intensified. Interestingly, the reduction rates appear to be very different for Cu-SACs-1 N-CQDs and Cu-SACs-3N-CQDs. Previous Cu-N-C electrocatalyst studies have also showed that the dynamic and reversible transition of Cu oxidation states from +II to 0 (neighboring Cu−Cu atom coordination) as real active sites with applied negative potentials affect the surface charge and consequently affect their catalytic activity, similar like our results.[51–55] Nevertheless, the reduction of cationic Cu single atom species to metallic Cu−Cu atom
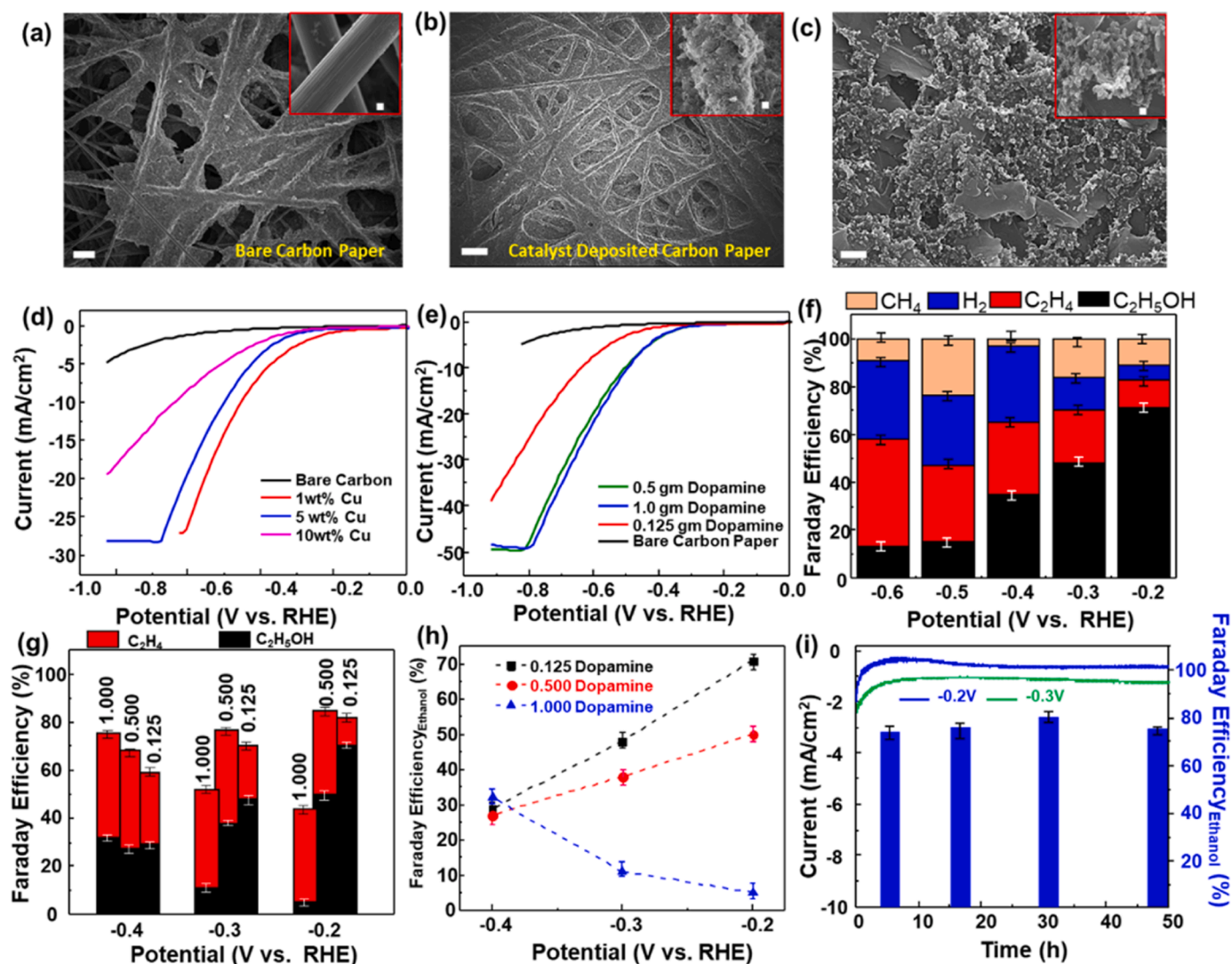
Fig. 6. (a) The bare carbon paper, (b) & (c) catalyst deposited carbon paper, (d) linear sweep voltammetry with different Cu wt%, (e) linear sweep voltammetry with different dopamine contents, (f) Faraday efficiency at different potential with 0.125 dopamine (Cu–SACs–1 N–CQDs), (g) & (h) Faraday efficiency of ethanol with different dopamine contents (0.125-Cu–SACs–1 N–CQDs,0.500-Cu–SACs–2 N–CQDs,1.000-Cu–SACs–3 N–CQDs), (i) 50 h chronoamperometry stability with Faraday efficiency (scale bar: (a) 50 μm, (b) 100 μm, (c) 1 μm, inset of (a, b) 1 μm (c) 100 nm).

coordination takes place under applied negative potential, and this transition is reversible upon removing the applied potential. Consequently, determining the size and morphology of the resulting metallic Cu cluster (Cu-Cu) poses a challenge.

The rational engineering of the coordination environment and electronic structure of single metal atoms intricately influences the reactivity of the active site, enabling control over catalytic activity, product selectivity, and stability. In our study, the atomic structure of Cu atoms influences the catalytic activity and electrochemical CO_2 RR products. In agreement with XANES data, FT-EXAFS spectrum clearly indicated the reduction of cationic Cu species and the interaction between the neighboring Cu−Cu atom coordination driven by the applied potentials during electrochemical CO_2 reduction.[56] It is thus very likely that isolated Cu single atoms are the catalytically active species for CO_2 reduction. Based on the experimental results, we can draw a reliable conclusion that neighboring Cu−Cu atom coordination concurrently takes place in Cu-SACs-1 N-CQDs during CO_2 reduction reaction, which favored the ethanol production over ethylene at low overpotential (−0.2 V). Although at higher potential, Cu-SACs-1 N-CQDs exhibited a high fraction of Cu-N moieties and Cu-O moieties, which favored the ethylene formation over ethanol. In the case of Cu-SACs-3 N-CQDs,

ex-situ presence of CuO_x atomic clusters dispersion dominants the ethylene formation as compared to ethanol. Overall, the reduction of isolated Cu single atoms to metallic neighboring Cu−Cu atom coordination active sites can promote generation of ethanol production in CO_2RR. Previous study[23,27,52,55] also showed that the synergistic effect of isolated to Cu metallic active sites could promote generation of C_2 products, although the selectivity of C_2 products was low. Also, it was demonstrated that reversible cluster formation occurs in Cu-SACs under CO_2RR conditions give rise to higher ethanol selectivity [24].

This observation confirms that the modification of the Cu coordination environment significantly hinders C–O bond breaking and stabilizes intermediates, favoring the production of ethanol over ethylene. When Cu single atoms are in close proximity to each other, a synergistic effect emerges between adjacent Cu single atoms, promoting the dimerization of *CO intermediates and facilitating the formation of C_{2+} products, such as ethanol and ethylene. [57,58] The pathways for ethanol and ethylene production share similarities on Cu atoms, commencing with the dimerization of two adsorbed–CO species, followed by multiple steps of protonation and dehydration, resulting in a common intermediate. Crucially, the selectivity between ethanol and ethylene is heavily contingent on the relative stabilities of subsequent
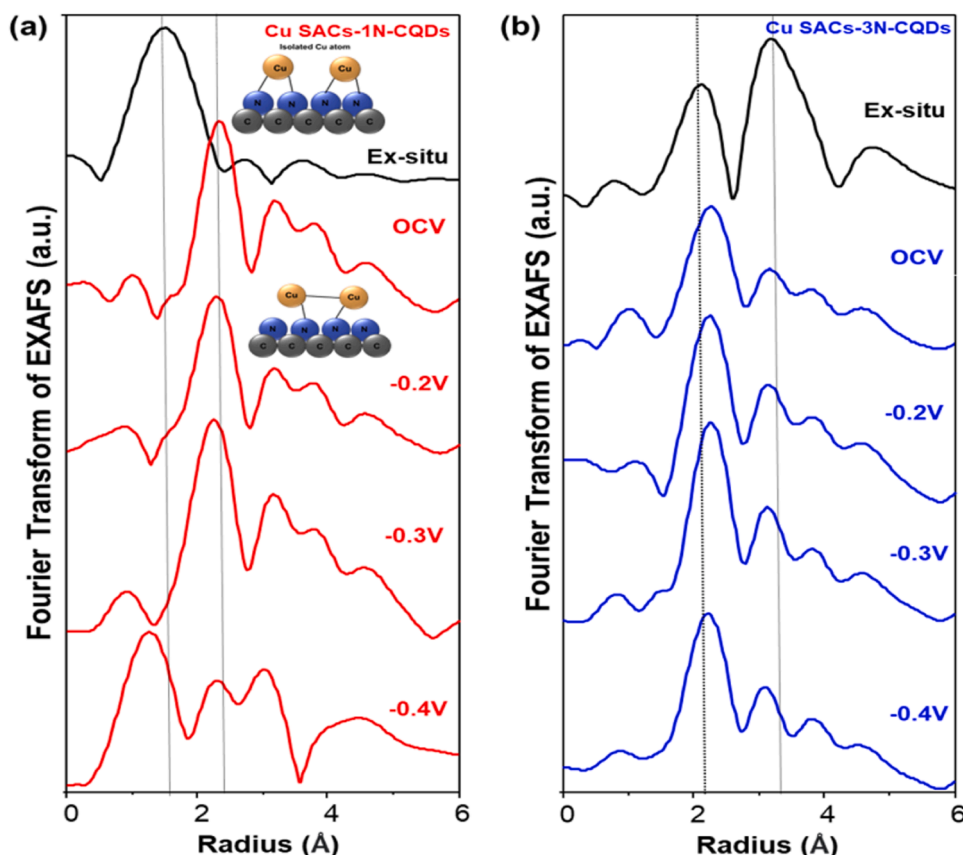
Fig. 7. *Operando* XAS characterization of the (a) Cu–SACs–1 N–CQDs, (b) Cu–SACs–3 N–CQDs recorded at different potentials in CO_2 reduction.

intermediates branching from *HCCOH on Cu sites [59] Copper with a surface featuring relatively low coordination and an optimal oxide state proves advantageous for ethanol generation over ethylene. This preference arises from the fact that the reaction intermediates for ethanol exhibit higher saturation compared to those for ethylene, and the existing oxidation state facilitates the binding of crucial oxygen-bound intermediates crucial for ethanol production. DFT calculations on Cu SACs catalyst also evidenced that the transient Cu clusters formed in situ from Cu single atoms and linked to the surface hydroxyl group were acts as active sites, which controlled the HCOO* pathways to become the main generation path of ethanol. In HCOO* pathways, absorbed CO_2 (*CO_2) goes through surface hydrogenation and desorbs as *HCOO intermediate and then reacts with other adsorbed species to form ethanol ($CO_2 \rightarrow CO_2$
*$\rightarrow CO* \rightarrow COOH* \rightarrow OCCO* \rightarrow OCCOH* \rightarrow OCC* \rightarrow OCCH* \rightarrow OCCH_2$
*$\rightarrow OCCH_3 * \rightarrow OCHCH_3 * \rightarrow HOCHCH_3 * \rightarrow HOCH_2CH_3 * \rightarrow C_2H_5OH$) [56,60,61].

As a result, a mechanism for enhanced ethanol production on Cu-SACs-1 N-CQDs can be postulated. Initially, the coordinated Cu single atom surface establishes connections with neighboring Cu atoms under a negative bias. Subsequently, the Cu-Cu induced moderate coordination numbers and optimal oxidation state of the Cu surface regulated the binding strength of *CO, leading to asymmetric C–C coupling. Due to the relatively low oxygen affinity and unsaturated nature of the ethylene intermediates compared to ethanol, the asymmetric C–C coupling creates an imbalanced coordination environment that favors the formation and stabilization of ethanol intermediates at a lower energy level than that for ethylene. This imbalance facilitates the pathway for ethanol production. Our low temperature electrocatalyst strategy revealed the switch of the reaction path from ethanol to ethylene as well as the switch in the selectivity with applied potential. Coincidently, both the FE activity and selectivity to ethanol production arrive at the highest values at

the potential of − 0.20 V versus RHE. This may lead to a conclusion that the neighboring metallic Cu−Cu atom coordination is more active and favorable for ethanol production.

It is interesting that an increase in dopamine results in a decrease in Cu single atoms, implying that the electronic structure is predominantly influenced by the local coordination chemistry of single atoms with the surrounding donor atoms from the support, resembling the metal-ligand interaction. Furthermore, when correlating the real structure with catalytic activity, a relationship between structural features and CO_2 reduction performance becomes apparent. Specifically, a lower coordination number of Cu (isolated single atoms) corresponds to a lower oxidation state of Cu single atoms, resulting in higher catalytic activity for ethanol production. Conversely, a larger coordination number (Cu atomic clusters) leads to decreased ethanol production. This structure-activity relationship underscores that the catalytic performance of single-atom catalysts (SACs) can be finely tuned and optimized by altering the local coordination environment, akin to modifying the ligand of catalysts. Through this approach, a coordination structure-performance relationship can be established by correlating CO_2 reduction catalytic activity with the coordination structure of Cu-SACs-N-CQDs. As dopamine content increases, the FE of ethanol gradually decreases, indicating that increased Cu clustering can suppress ethanol production under Cu clustering conditions due to changes in the coordination environment.

A techno-economic analysis (TEA) model for a CO_2 electrolyzer system was calculated to the ethanol as the production material and energy balances for the process, estimated the capital investment, operating costs, and net present value. Based on the CO_2 mass flow rate, the materials and energy necessary for ethanol production are quantified, forming the basis for estimating both capital and operating expenses. The TEA relies on key process and economic assumptions, which are outlined in the Supplementary information. To approximate the

capital costs of an electrolyzer system, a representative model, specifically an alkaline water electrolyzer stack, was employed based on findings from a previous study [62,63].

4. Conclusions

In summary, we present a facile metal–amine (Cu–dopamine) complex and low-temperature (160 °C) hydrothermal strategy to synthesize the Cu–SACs–N–CQDs electrocatalyst containing atomically dispersed isolated Cu atoms on N-doped carbon dots supports (2–6 nm). Also, the Cu metal coordination and local environment loading can be controlled through the variation in dopamine contents. Moreover, the atomically dispersed Cu–SACs–N–CQDs solutions are stable enough for a long time of over six months, showing their stability. The transmission electron microscopy and extended X-ray absorption fine structure spectroscopy (EXAFS) confirm that the isolated Cu atoms are uniformly dispersed over an N-doped carbons dots support. Owing to the unique local atomic structure and good dispersion of the isolated Cu atom on N–CQDs, the optimized Cu–SACs–1 N–CQDs electrocatalyst is demonstrated to be highly efficient and highly selective towards the formation of ethanol during electrocatalytic CO_2 reduction. The synthesized Cu–SACs–1 N–CQDs catalyst exhibits improved Faraday efficiency (> 80%) for boosted ethanol production and decreased ethylene formation at low overpotential (-0.2 V vs. RHE) in aqueous 0.1 M $KHCO_3$ electrolytes with 50 h stability. With increased dopamine contents during synthesis, the Cu–SACs–2 N–CQDs and Cu–SACs–3 N–CQDs demonstrate selectivity towards the formation of ethylene. At -0.2 V vs. RHE for the best CO_2RR performance to ethanol, the *operando* XANES spectrum of the Cu–SACs–1 N–CQDs electrode exhibits the best similarity, which we regard as the ideal electronic structure of the Cu–SACs–1 N–CQDs for the CO_2 RR. These real-time mimicked XANES results clearly demonstrate the evolution of neighboring Cu–Cu atom coordination as active species from isolated Cu atoms during CO_2 reduction reaction, which favors the ethanol formation. Our work illustrates the great potential of Cu–SACs for the development of CO_2 electroreduction to ethanol at low overpotential, as well as the switch of the reaction path from ethanol to ethylene.

CRediT authorship contribution statement

Baik Jeong Min: Supervision, Writing – review & editing. **Choi Jae Young:** Investigation, Writing – review & editing. **Oh Hyung-Suk:** Investigation, Writing – review & editing. **Choi Sung Yeol:** Data curation. **Woo Chae Heon:** Data curation. **Purbia Rahul:** Conceptualization, Formal analysis, Investigation, Methodology, Writing – original draft. **Jeon Jiho:** Data curation. **Lim Chul Wan:** Formal analysis, Methodology. **Lee Dong Ki:** Data curation.

Declaration of Competing Interest

The authors declare that they have no known competing financial interests or personal relationships that could have appeared to influence the work reported in this paper.

Data Availability

Data will be made available on request.

Acknowledgments

Appendix A. Supplementary data

[Supplementary material](#) related to this article can be found. The [Supplementary Information](#) includes TEM images, EDS, Raman spectra, NMR, GC and XANES spectra.

Appendix A. Supporting information

Supplementary data associated with this article can be found in the online version at [doi:10.1016/j.apcatb.2024.123694](https://doi.org/10.1016/j.apcatb.2024.123694).

References

[1] S. Nitopi, E. Bertheussen, S.B. Scott, X. Liu, A.K. Engstfeld, S. Horch, B. Seger, I.E.L. Stephens, K. Chan, C. Hahn, J.K. Nørskov, T.F. Jaramillo, I. Chorkendorff, Progress and perspectives of electrochemical CO_2 reduction on copper in aqueous electrolyte, Chem. Rev. 119 (2019) 7610–7672, https://doi.org/10.1021/acs.chemrev.8b00705.

[2] R. Francke, B. Schille, M. Roemelt, Homogeneously catalyzed electroreduction of carbon dioxide—methods, mechanisms, and catalysts, Chem. Rev. 118 (2018) 4631–4701, https://doi.org/10.1021/acs.chemrev.7b00459.

[3] C.-T. Dinh, T. Burdyny, M.G. Kibria, A. Seifitokaldani, C.M. Gabardo, F.P. García de Arquer, A. Kiani, J.P. Edwards, P. De Luna, O.S. Bushuyev, C. Zou, R. Quintero-Bermudez, Y. Pang, D. Sinton, E.H. Sargent, CO_2 electroreduction to ethylene via hydroxide-mediated copper catalysis at an abrupt interface, Science 360 (2018) 783–787, https://doi.org/10.1126/science.aas9100.

[4] X. Tan, C. Yu, Y. Ren, S. Cui, W. Li, J. Qiu, Recent advances in innovative strategies for the CO_2 electroreduction reaction, Energy Environ. Sci. 14 (2021) 765–780, https://doi.org/10.1039/D0EE02981E.

[5] W. Deng, P. Zhang, B. Seger, J. Gong, Unraveling the rate-limiting step of two-electron transfer electrochemical reduction of carbon dioxide, Nat. Commun. 13 (2022) 803, https://doi.org/10.1038/s41467-022-28436-z.

[6] Q. Zhao, J.M.P. Martirez, E.A. Carter, Revisiting understanding of electrochemical CO_2 reduction on Cu(111): competing proton-coupled electron transfer reaction mechanisms revealed by embedded correlated wavefunction theory, J. Am. Chem. Soc. 143 (2021) 6152–6164, https://doi.org/10.1021/jacs.1c00880.

[7] A.J. Göttle, M.T.M. Koper, Proton-coupled electron transfer in the electrocatalysis of CO_2 reduction: prediction of sequential vs. concerted pathways using DFT, Chem. Sci. 8 (2017) 458–465, https://doi.org/10.1039/C6SC02984A.

[8] S.R. Hui, P. De Luna, How increasing proton and electron conduction benefits electrocatalytic CO_2 reduction, Matter 4 (2021) 1555–1577, https://doi.org/10.1016/j.matt.2021.02.021.

[9] Z. Ma, Z. Yang, W. Lai, Q. Wang, Y. Qiao, H. Tao, C. Lian, M. Liu, C. Ma, A. Pan, H. Huang, CO_2 electroreduction to multicarbon products in strongly acidic electrolyte via synergistically modulating the local microenvironment, Nat. Commun. 13 (2022) 7596, https://doi.org/10.1038/s41467-022-35415-x.

[10] B. Yang, K. Liu, H. Li, C. Liu, J. Fu, H. Li, J.E. Huang, P. Ou, T. Alkayyali, C. Cai, Y. Duan, H. Liu, P. An, N. Zhang, W. Li, X. Qiu, C. Jia, J. Hu, L. Chai, Z. Lin, Y. Gao, M. Miyauchi, E. Cortés, S.A. Maier, M. Liu, Accelerating CO_2 electroreduction to multicarbon products via synergistic electric–thermal field on copper nanoneedles, J. Am. Chem. Soc. 144 (2022) 3039–3049, https://doi.org/10.1021/jacs.1c11253.

[11] X. Zhang, J. Li, Y.-Y. Li, Y. Jung, Y. Kuang, G. Zhu, Y. Liang, H. Dai, Selective and high current CO_2 electro-reduction to multicarbon products in near-neutral KCl electrolytes, J. Am. Chem. Soc. 143 (2021) 3245–3255, https://doi.org/10.1021/jacs.0c13427.

[12] H. Xu, D. Rebollar, H. He, L. Chong, Y. Liu, C. Liu, C.-J. Sun, T. Li, J.V. Muntean, R.E. Winans, D.-J. Liu, T. Xu, Highly selective electrocatalytic CO_2 reduction to ethanol by metallic clusters dynamically formed from atomically dispersed copper, Nat. Energy 5 (2020) 623–632, https://doi.org/10.1038/s41560-020-0666-x.

[13] Z. Gu, H. Shen, Z. Chen, Y. Yang, C. Yang, Y. Ji, Y. Wang, C. Zhu, J. Liu, J. Li, T.-K. Sham, X. Xu, G. Zheng, Efficient electrocatalytic CO_2 reduction to C_{2+} alcohols at defect-site-rich Cu surface, Joule 5 (2021) 429–440, https://doi.org/10.1016/j.joule.2020.12.011.

[14] C. Zhou, A.S. Asundi, E.D. Goodman, J. Hong, B. Werghi, A.S. Hoffman, S.S. Nathan, S.F. Bent, S.R. Bare, M. Cargnello, Steering CO_2 hydrogenation toward C-C coupling to hydrocarbons using porous organic polymer/metal interfaces, Proc. Natl. Acad. Sci. USA 119 (2022), https://doi.org/10.1073/pnas.2114768119.

[15] D. Ren, Y. Deng, A.D. Handoko, C.S. Chen, S. Malkhandi, B.S. Yeo, Selective electrochemical reduction of carbon dioxide to ethylene and ethanol on Copper(I) oxide catalysts, ACS Catal. 5 (2015) 2814–2821, https://doi.org/10.1021/cs502128q.

[16] Y. Kwon, Y. Lum, E.L. Clark, J.W. Ager, A.T. Bell, CO_2 electroreduction with enhanced ethylene and ethanol selectivity by nanostructuring polycrystalline copper, ChemElectroChem 3 (2016) 1012–1019, https://doi.org/10.1002/celc.201600068.

[17] S. Ma, M. Sadakiyo, R. Luo, M. Heima, M. Yamauchi, P.J.A. Kenis, One-step electrosynthesis of ethylene and ethanol from CO_2 in an alkaline electrolyzer, J. Power Sources 301 (2016) 219–228, https://doi.org/10.1016/j.jpowsour.2015.09.124.

[18] Z.W. Seh, J. Kibsgaard, C.F. Dickens, I. Chorkendorff, J.K. Nørskov, T.F. Jaramillo, Combining theory and experiment in electrocatalysis: Insights into materials design, Science 355 (2017) eaad4998, https://doi.org/10.1126/science.aad4998.

[19] S.Y. Lee, H. Jung, N.-K. Kim, H.-S. Oh, B.K. Min, Y.J. Hwang, Mixed copper states in anodized Cu electrocatalyst for stable and selective ethylene production from CO₂ reduction, J. Am. Chem. Soc. 140 (2018) 8681–8689, https://doi.org/10.1021/jacs.8b02173.

[20] A. Loiudice, P. Lobaccaro, E.A. Kamali, T. Thao, B.H. Huang, J.W. Ager, R. Buonsanti, Tailoring copper nanocrystals towards C₂ products in electrochemical CO₂ reduction, Angew. Chem. Int. Ed. 55 (2016) 5789–5792, https://doi.org/10.1002/anie.201601582.

[21] A. Thevenon, A. Rosas-Hernández, J.C. Peters, T. Agapie, In-situ nanostructuring and stabilization of polycrystalline copper by an organic salt additive promotes electrocatalytic CO₂ reduction to ethylene, Angew. Chem. Int. Ed. 58 (2019) 16952–16958, https://doi.org/10.1002/anie.201907935.

[22] J.H. Montoya, A.A. Peterson, J.K. Nørskov, Insights into C-C coupling in CO₂ electroreduction on copper electrodes, ChemCatChem 5 (2013) 737–742, https://doi.org/10.1002/cctc.201200564.

[23] Y. Cai, J. Fu, Y. Zhou, Y.-C. Chang, Q. Min, J.-J. Zhu, Y. Lin, W. Zhu, Insights on forming N,O-coordinated Cu single-atom catalysts for electrochemical reduction CO₂ to methane, Nat. Commun. 12 (2021) 586, https://doi.org/10.1038/s41467-020-20769-x.

[24] C.E. Creissen, M. Fontecave, Keeping sight of copper in single-atom catalysts for electrochemical carbon dioxide reduction, Nat. Commun. 13 (2022) 2280, https://doi.org/10.1038/s41467-022-30027-x.

[25] J. Zhang, W. Cai, F.X. Hu, H. Yang, B. Liu, Recent advances in single atom catalysts for the electrochemical carbon dioxide reduction reaction, Chem. Sci. 12 (2021) 6800–6819, https://doi.org/10.1039/D1SC01375K.

[26] S. Kuang, Y. Su, M. Li, H. Liu, H. Chuai, X. Chen, E.J.M. Hensen, T.J. Meyer, S. Zhang, X. Ma, Asymmetrical electrohydrogenation of CO₂ to ethanol with copper–gold heterojunctions, Proc. Natl. Acad. Sci. 120 (2023) e2214175120, https://doi.org/10.1073/pnas.2214175120.

[27] X. Su, Z. Jiang, J. Zhou, H. Liu, D. Zhou, H. Shang, X. Ni, Z. Peng, F. Yang, W. Chen, Z. Qi, D. Wang, Y. Wang, Complementary operando spectroscopy identification of in-situ generated metastable charge-asymmetry Cu₂-CuN₃ clusters for CO₂ reduction to ethanol, Nat. Commun. 13 (2022) 1322, https://doi.org/10.1038/s41467-022-29035-8.

[28] S.H. Lee, J.C. Lin, M. Farmand, A.T. Landers, J.T. Feaster, J.E. Avilés Acosta, J. W. Beeman, Y. Ye, J. Yano, A. Mehta, R.C. Davis, T.F. Jaramillo, C. Hahn, W. S. Drisdell, Oxidation state and surface reconstruction of Cu under CO₂ reduction conditions from in situ X-ray characterization, J. Am. Chem. Soc. 143 (2021) 588–592, https://doi.org/10.1021/jacs.0c10017.

[29] T.-C. Chou, C.-C. Chang, H.-L. Yu, W.-Y. Yu, C.-L. Dong, J.-J. Velasco-Vélez, C.-H. Chuang, L.-C. Chen, J.-F. Lee, J.-M. Chen, H.-L. Wu, Controlling the oxidation state of the Cu electrode and reaction intermediates for electrochemical CO₂ reduction to ethylene, J. Am. Chem. Soc. 142 (2020) 2857–2867, https://doi.org/10.1021/jacs.9b11126.

[30] M.B. Gawande, P. Fornasiero, R. Zbořil, Carbon-based single-atom catalysts for advanced applications, ACS Catal. 10 (2020) 2231–2259, https://doi.org/10.1021/acscatal.9b04217.

[31] X.-L. Lu, X. Rong, C. Zhang, T.-B. Lu, Carbon-based single-atom catalysts for CO₂ electroreduction: progress and optimization strategies, J. Mater. Chem. A 8 (2020) 10695–10708, https://doi.org/10.1039/D0TA01955K.

[32] G. Qu, K. Wei, K. Pan, J. Qin, J. Lv, J. Li, P. Ning, Emerging materials for electrochemical CO₂ reduction: progress and optimization strategies of carbon-based single-atom catalysts, Nanoscale 15 (2023) 3666–3692, https://doi.org/10.1039/D2NR06190B.

[33] C. Xia, Y. Qiu, Y. Xia, P. Zhu, G. King, X. Zhang, Z. Wu, J.Y. Kim, D.A. Cullen, D. Zheng, P. Li, M. Shakouri, E. Heredia, P. Cui, H.N. Alshareef, Y. Hu, H. Wang, General synthesis of single-atom catalysts with high metal loading using graphene quantum dots, Nat. Chem. 13 (2021) 887–894, https://doi.org/10.1038/s41557-021-00734-x.

[34] J. Leverett, T. Tran-Phu, J.A. Yuwono, P. Kumar, C. Kim, Q. Zhai, C. Han, J. Qu, J. Cairney, A.N. Simonov, R.K. Hocking, L. Dai, R. Daiyan, R. Amal, Tuning the coordination structure of Cu-N-C single atom catalysts for simultaneous electrochemical reduction of CO₂ and NO₃ to urea, Adv. Energy Mater. 12 (2022) 2201500, https://doi.org/10.1002/aenm.202201500.

[35] C. Tang, A.-E. Surkus, F. Chen, M.-M. Pohl, G. Agostini, M. Schneider, H. Junge, M. Beller, A stable nanocobalt catalyst with highly dispersed CoNx active sites for the selective dehydrogenation of formic acid, Angew. Chem. Int. Ed. 56 (2017) 16616–16620, https://doi.org/10.1002/anie.201710766.

[36] H. Yang, L. Shang, Q. Zhang, R. Shi, G.I.N. Waterhouse, L. Gu, T. Zhang, A universal ligand mediated method for large scale synthesis of transition metal single atom catalysts, Nat. Commun. 10 (2019) 4585, https://doi.org/10.1038/s41467-019-12510-0.

[37] Y. Zhang, S. Ye, M. Gao, Y. Li, X. Huang, J. Song, H. Cai, Q. Zhang, J. Zhang, N-Doped graphene supported Cu single atoms: highly efficient recyclable catalyst for enhanced C-N coupling reactions, ACS Nano 16 (2022) 1142–1149, https://doi.org/10.1021/acsnano.1c08898.

[38] G.G. Mohamed, F.A. Nour El-Dien, R.G. El-Nahas, New copper(II) complexes with dopamine hydrochloride and vanillylmandelic acid: Spectroscopic and thermal characterization, Spectrochim. Acta Part A: Mol. Biomol. Spectrosc. 81 (2011) 489–497, https://doi.org/10.1016/j.saa.2011.06.042.

[39] M. Sys, A. Mukherjee, G. Jashari, Vc Adam, A.M. Ashrafi, M. Nováik, L.Å. Richtera, Bis(2,2′-bipyridil)Copper(II) chloride complex: tyrosinase biomimetic catalyst or redox mediator? Materials (2021) https://doi.org/10.3390/ma14010113.

[40] A.P. Sandoval-Rojas, L. Ibarra, M.T. Cortes, M.A. Macias, L. Suescun, J. Hurtado, Synthesis and characterization of copper(II) complexes containing acetate and N,N-donor ligands, and their electrochemical behavior in dopamine detection,

[41] R. Griesser, H. Sigel, Ternary complexes in solution. VIII. Complex formation between the copper(II)-2,2′-bipyridyl 1:1 complex and ligands containing oxygen and/or nitrogen donor atoms, Inorg. Chem. 9 (1970) 1238–1243, https://doi.org/10.1021/ic50087a045.

[42] J.N. Hamann, R. Schneider, F. Tuczek, Catalytic oxygenation of various monophenols by copper(I) complexes with bis(pyrazolyl)methane ligands: differences in reactivity, J. Coord. Chem. 68 (2015) 3259–3271, https://doi.org/10.1080/00958972.2015.1074191.

[43] B.J. Sanghavi, S.M. Mobin, P. Mathur, G.K. Lahiri, A.K. Srivastava, Biomimetic sensor for certain catecholamines employing copper(II) complex and silver nanoparticle modified glassy carbon paste electrode, Biosens. Bioelectron. 39 (2013) 124–132, https://doi.org/10.1016/j.bios.2012.07.008.

[44] S. Sheik Mansoor, Mixed metal complexes of copper (II), nickel (II) and zinc (II) involving dopa and dopamine, Int. J. ChemTech Res 2 (2010) 640–645.

[45] W. Zheng, H. Fan, L. Wang, Z. Jin, Oxidative Self-Polymerization of Dopamine in an Acidic Environment, Langmuir 31 (2015) 11671–11677, https://doi.org/10.1021/acs.langmuir.5b02757.

[46] N. Gong, X. Ma, X. Ye, Q. Zhou, X. Chen, X. Tan, S. Yao, S. Huo, T. Zhang, S. Chen, X. Teng, X. Hu, J. Yu, Y. Gan, H. Jiang, J. Li, X.-J. Liang, Carbon-dot-supported atomically dispersed gold as a mitochondrial oxidative stress amplifier for cancer treatment, Nat. Nanotechnol. 14 (2019) 379–387, https://doi.org/10.1038/s41565-019-0373-6.

[47] Y. Lee, T.G. Park, Facile fabrication of branched gold nanoparticles by reductive hydroxyphenol derivatives, Langmuir 27 (2011) 2965–2971, https://doi.org/10.1021/la1044078.

[48] Y. Ma, H. Niu, X. Zhang, Y. Cai, One-step synthesis of silver/dopamine nanoparticles and visual detection of melamine in raw milk, Analyst 136 (2011) 4192–4196, https://doi.org/10.1039/C1AN15327G.

[49] M.D. Shultz, J.U. Reveles, S.N. Khanna, E.E. Carpenter, Reactive nature of dopamine as a surface functionalization agent in iron oxide nanoparticles, J. Am. Chem. Soc. 129 (2007) 2482–2487, https://doi.org/10.1021/ja0651963.

[50] M. Akagawa, Y. Ishii, T. Ishii, T. Shibata, M. Yotsu-Yamashita, K. Suyama, K. Uchida, Metal-catalyzed oxidation of protein-bound dopamine, Biochemistry 45 (2006) 15120–15128, https://doi.org/10.1021/bi0614434.

[51] D. Karapinar, N.T. Huan, N. Ranjbar Sahraie, J. Li, D. Wakerley, N. Touati, S. Zanna, D. Taverna, L.H. Galvao Tizei, A. Zitolo, Fdr Jaouen, V. Mougel, M. Fontecave, Electroreduction of CO₂ on single-site copper-nitrogen-doped carbon material: selective formation of ethanol and reversible restructuration of the metal sites, Angew. Chem. Int. Ed. 58 (2019) 15098–15103, https://doi.org/10.1002/anie.201907994.

[52] Z. Weng, Y. Wu, M. Wang, J. Jiang, K. Yang, S. Huo, X.-F. Wang, Q. Ma, G. W. Brudvig, V.S. Batista, Y. Liang, Z. Feng, H. Wang, Active sites of copper-complex catalytic materials for electrochemical carbon dioxide reduction, Nat. Commun. 9 (2018) 415, https://doi.org/10.1038/s41467-018-02819-7.

[53] J. Jin, J. Wicks, Q. Min, J. Li, Y. Hu, J. Ma, Y. Wang, Z. Jiang, Y. Xu, R. Lu, G. Si, P. Papangelakis, M. Shakouri, Q. Ou, P. Ou, X. Wang, Z. Chen, W. Zhang, K. Yu, J. Song, X. Jiang, P. Qiu, Y. Lou, D. Wu, Y. Mao, A. Ozden, C. Wang, C. Xia, X. Hu, V.P. Dravid, Y.-M. Yiu, T.-K. Sham, Z. Wang, D. Sinton, L. Mai, E.H. Sargent, Y. Pang, Constrained C₂ adsorbate orientation enables CO-to-acetate electroreduction, Nature 617 (2023) 724–729, https://doi.org/10.1038/s41586-023-05918-8.

[54] W. Fu, J. Wan, H. Zhang, J. Li, W. Chen, Y. Li, Z. Guo, Y. Wang, Photoinduced loading of electron-rich Cu single atoms by moderate coordination for hydrogen evolution, Nat. Commun. 13 (2022) 5496, https://doi.org/10.1038/s41467-022-33275-z.

[55] P. De Luna, R. Quintero-Bermudez, C.-T. Dinh, M.B. Ross, O.S. Bushuyev, P. Todorovi, T. Regier, S.O. Kelley, P. Yang, E.H. Sargent, Catalyst electro-redeposition controls morphology and oxidation state for selective carbon dioxide reduction, Nat. Catal. 1 (2018) 103–110, https://doi.org/10.1038/s41929-017-0018-9.

[56] X. Bai, X. Zhao, Y. Zhang, C. Ling, Y. Zhou, J. Wang, Y. Liu, Dynamic stability of copper single-atom catalysts under working conditions, J. Am. Chem. Soc. 144 (2022) 17140–17148, https://doi.org/10.1021/jacs.2c07178.

[57] K. Zhao, X. Nie, H. Wang, S. Chen, X. Quan, H. Yu, W. Choi, G. Zhang, B. Kim, J. G. Chen, Selective electroreduction of CO₂ to acetone by single copper atoms anchored on N-doped porous carbon, Nat. Commun. 11 (2020) 2455, https://doi.org/10.1038/s41467-020-16381-8.

[58] A. Guan, Z. Chen, Y. Quan, C. Peng, Z. Wang, T.-K. Sham, C. Yang, Y. Ji, L. Qian, X. Xu, G. Zheng, Boosting CO₂ electroreduction to CH₄ via tuning neighboring single-copper sites, ACS Energy Lett. 5 (2020) 1044–1053, https://doi.org/10.1021/acsenergylett.0c00018.

[59] P. Wang, H. Yang, C. Tang, Y. Wu, Y. Zheng, T. Cheng, K. Davey, X. Huang, S.-Z. Qiao, Boosting electrocatalytic CO₂toethanol production via asymmetric CC coupling, Nat. Commun. 13 (2022) 3754, https://doi.org/10.1038/s41467-022-31427-9.

[60] W. Xia, Y. Xie, S. Jia, S. Han, R. Qi, T. Chen, X. Xing, T. Yao, D. Zhou, X. Dong, J. Zhai, J. Li, J. He, D. Jiang, Y. Yamauchi, M. He, H. Wu, B. Han, Adjacent copper single atoms promote CC coupling in electrochemical CO₂ reduction for the efficient conversion of ethanol, J. Am. Chem. Soc. 145 (2023) 17253–17264, https://doi.org/10.1021/jacs.3c04612.

[61] J. Wang, D. Deng, Q. Wu, M. Liu, Y. Wang, J. Jiang, X. Zheng, H. Zheng, Y. Bai, Y. Chen, X. Xiong, Y. Lei, Insight on atomically dispersed Cu catalysts for

electrochemical CO$_2$ reduction, ACS Nano (2023), https://doi.org/10.1021/acsnano.3c07307.

[62] M. Jouny, W. Luc, F. Jiao, General techno-economic analysis of CO$_2$ electrolysis systems, Ind. Eng. Chem. Res. 57 (2018) 2165–2177, https://doi.org/10.1021/acs.iecr.7b03514.

[63] J. Na, B. Seo, J. Kim, C.W. Lee, H. Lee, Y.J. Hwang, B.K. Min, D.K. Lee, H.-S. Oh, U. Lee, General technoeconomic analysis for electrochemical coproduction coupling carbon dioxide reduction with organic oxidation, Nat. Commun. 10 (2019) 5193, https://doi.org/10.1038/s41467-019-12744-y.